# Computational design of a crack-free aluminum alloy for additive manufacturing

Alixe Dreano, Julien Favre, Christophe Desrayaud, Pauline Chanin-Lambert, Andreas Wimmer, Michael F. Zaeh

# Computational design of a crack-free aluminum alloy for additive manufacturing

Alixe Dreano[1], Julien Favre[1*], Christophe Desrayaud[1], Pauline Chanin-Lambert[1], Andreas Wimmer[2], Michael F. Zaeh[2]

[1] Mines Saint-Etienne, Université Lyon, CNRS, UMR 5307 LGF, Centre SMS, Département PMM, F 42023 Saint-Etienne, France

[2] Technical University of Munich, TUM School of Engineering and Design, Institute for Machine Tools and Industrial Management, Boltzmannstr. 15, 85748 Garching, Germany

[*]julien.favre@emse.fr

## Abstract

The design of new alloys adapted to LPBF and combining suitable mechanical strength together with a low cracking susceptibility is a promising way to produce defect-free parts made of aluminum. The current work proposes a design procedure relying on the decrease of the brittle temperature range to mitigate the hot cracking issue and additional optimization criteria concerning the phases fractions and the solid solution strengthening to preserve the mechanical strength and some ductility. The optimization functions are included in an aggregated genetic algorithm for a rapid and efficient identification of the optimal composition. The algorithm determined a promising alloy, with a brittle temperature range of only 9°C, and mostly constituted of FCC phase (around 90%), with some $Mg_2Si$ and $Al_9FeNi$ precipitates. The alloy is found suitable for the LPBF process with no cracks observed. Hence, the criterion for the mitigation of hot cracking is validated. Mechanical results shown a high yield stress and ultimate trensile stress but an elongation at break quite low compared to conventional manufactured aluminum alloys.

## Keywords

Alloy design ; Aluminum alloy ; Hot-cracking ; Laser-powder bed fusion ; Microstructure

## 1. Introduction

Aluminum alloys present a growing interest for laser additive manufacturing due to their low density and their high specific strength. However their application is limited by numerous defects induced by the Laser Powder Bed Fusion (LPBF) process: cracks, porosities, balling, or surface roughness [1,2]. Indeed, the LPBF process is influenced by the physical properties of the aluminum alloys such as high reflectivity, oxidation, low boiling point, high thermal conductivity, high coefficient of thermal expansion, large solidification temperature range or loss of alloying elements during the process [1]. The major issue for the manufacturing of aluminum by LPBF is the occurrence of hot cracking. Hot cracking comes from the lack of liquid in the interdendritic spaces during the solidification shrinkage, and the impossibility for the solid to accommodate strain variations [3,4].

In a recent review, Galy and co-authors [2] showed that series 4XXX or 5XXX are less susceptible to crack during the LPBF process compared to 7XXX or 6XXX series, which, on the other side, present better mechanical properties. The presence of Si and Mn in 4XXX and 5XXX series induces a facility for welding due to the small difference between liquidus and solidus temperatures. In addition, silicon gives a better laser absorption and a good flowability to the alloy [2]. On the contrary, the well-known susceptibility of hot cracking during welding for high-strength aluminum alloys strongly limits their use for additive manufacturing. Yet, the presence of Cu, Mg, Si and Zn allow the possibility to improve the mechanical properties by heat treaments [2]. Hence, a growing interest is observed to produce crack-free additive manufactured aluminum alloys with high mechanical properties.

There are two strategies for the reduction of hot cracking. The first one is based on grain refinement by the addition of nucleating agents [5,6], resulting in better strain accommodation and higher resistance to cracking. For example, it was found that the addition of Sc and Zr in aluminum alloys improved its mechanical properties and reduced the occurrence of cracking by promoting the formation of equiaxed microstructure [5,7]. However, this technique is difficult to implement in a global optimization approach, because it would require a detailed thermokinetic model of the nucleation and growth during solidification to estimate the level of grain refinement. Such a model would require a significant amount of experimental work to set the parameters, and the benefits of using numerical optimization over experimental trial-and-error would be reduced.

The second strategy benefits from a eutectic solidification or the lowering of the solidification range [4,8]. A Brittle Temperature Range (BTR) could be defined as presenting the highest susceptibility for hot cracking to occur [9,10]. The BTR corresponds to the temperature at which the solid fraction is high enough to cause a loss of permeability of the liquid and to the temperature at which the solid fraction is sufficient to increase the mechanical resistance and to resist to strain variation [11]. Montero et al. [12] proposed to add silicon in 7075 to improve its weldability. By adding silicon, the BTR reduces and cracks are less easily formed during the process but the mechanical properties of the mix 7075 + 4 % Si are degraded compared to pure 7075. Casati and co-authors [13] also added Si in the composition of a high strength Al-Zn-Si-Mg-Cu powder thus reducing hot cracking during the LPBF process but by maintaining good mechanical properties.

Computational alloy design presents a growing interest since numerous tools are now available to strengthen the method. The use of numerical methods, such as the CALPHAD method, were successfully applied to predict microstructure, precipitation, and phases [14,15] and tend to increase significantly the size of the alloy design space. When the physically-based prediction is impossible,

statistical learning methods can be used to predict properties based on data available in the literature [16–18]. These predictive models are then implemented into an optimization algorithm, limiting the calculations and leading to the generation of interesting alloy compositions. Many optimization methods for materials science are based on metaheuristic algorithms such as mono-objective or multi-objective genetic algorithms [16–19]. This study aims to apply this method for additive manufacturing of aluminum alloys, as proposed elsewhere [20–22] for steels or Ni-based alloys. The final objective is then to design a new aluminum alloys exhibiting good mechanical properties and avoiding hot cracking during the LPBF process.

## 2. Computational alloy design

### 2.1 Reference alloys

In this work, the proposed design rules were tested on conventional alloys (AlSi10Mg, 6061, and 7075) to validate their relevance. The AlSi10Mg alloy is known to present a good weldability, thus avoiding hot cracking during the LPBF process. The weldability properties mainly come from the presence of Si (Table 1).

*Table 1: Composition of commercial alloys (wt.%)*

| | Si | Fe | Cu | Mn | Mg | Cr | Zn | Ti |
|---|---|---|---|---|---|---|---|---|
| AlSi10Mg | 10.00 | 0.50 | 0.03 | 0.40 | 0.35 | 0.00 | 0.10 | 0.15 |
| 6061 | 0.60 | 0.70 | 0.28 | 0.15 | 1.00 | 0.60 | 0.25 | 0.15 |
| 7075 | 0.40 | 0.50 | 1.21 | 0.30 | 2.50 | 0.23 | 5.60 | 0.20 |

Even if the mechanical properties of AlSi10Mg are enhanced by the LPBF process, they remain still low compared to the mechanical properties of 6061 and 7075 produced by conventional techniques (Table 2). However, the susceptibility of 6061 and 7075 to cracking during additive manufacturing induces bad mechanical properties compared to the one obtained by conventional processes (Table 2). The objective is then to propose an alloy exhibiting the same weldability as AlSi10Mg and mechanical properties as good as 6061 and 7075 produced by conventional ways.

*Table 2: Properties of AlSi10Mg, 7075 and 6061*

| | Yield stress (MPa) | | UTS (MPa) | | Elongation at break (%) | | Susceptibility to hot cracking [2] (- : not susceptible ; ++ very susceptible) |
|---|---|---|---|---|---|---|---|
| | Conventional [23] | AM (as-built) | Conventional [23] | AM (as-built) | Conventional [23] | AM (as-built) | |
| AlSi10Mg | 137 – 152 | 230 [24] – 264 [25] | 296 – 325 | 360 [24] – 482 [25] | 2.5 – 3 | 1 – 8.5 [24–26] | - |
| 6061 | 196 – 215 | 110 - 160 [27] | 247 – 287 | ~ 160 [27] | 12 – 18 | 1 – 3 [27] | + |
| 7075 | 326 – 440 | early failure [5] | 408 – 508 | 25.5 [5] | 5 – 8 | 0.4 [5,24] | ++ |

## 2.2 Controlling the solidification temperature range

Usually, the BTR is defined between the cohesion solid fraction and the coalescence solid fraction [10]. Since the chemical composition of the alloy influences the solidification range, it is proposed to optimize the alloy by considering that the BTR has to be as low as possible.

An objective is introduced on the value of $\Delta T$ in the optimisation process and is written as follows:

$$\Delta T = \left| T(f_{\mathrm{s,max}}) - T(f_{\mathrm{s,min}}) \right| \qquad (1)$$

where $f_{\mathrm{s,max}} = 0.97$ and $f_{\mathrm{s,min}} = 0.80$. The lower bound $f_{\mathrm{s,min}}$ was deliberately selected at a low value compared to the literature to provide a more selective criterion for the optimization, therefore limiting with a higher severity any possible occurrence of thermal straining. These solid fraction boundaries are also consistent with the work of Mishra et al. [28] who recently proposed to design a new LPBF aluminum alloy presenting an eutectic-like solidification in the terminal stage ($f_s$ > 0.40) of the solidification to lower hot-cracking susceptibility.

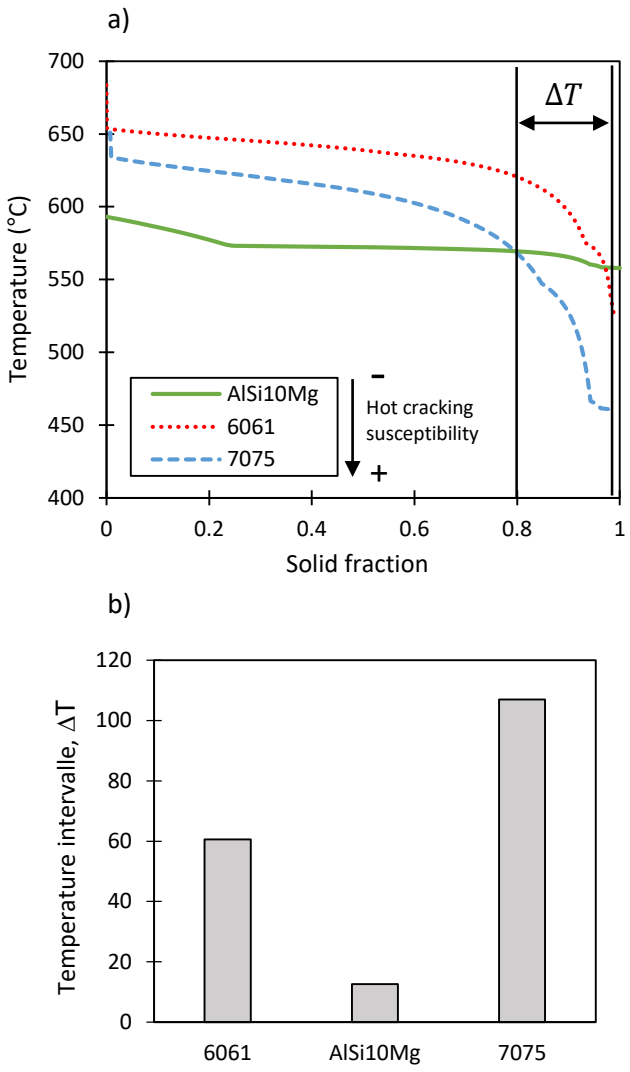


Figure 1: a) Scheil-Gulliver solidification model for AlSi10Mg, 6061, and 7075 aluminum alloys; b) comparison of the calculated $\Delta T$

The Scheil-Gulliver model was adopted in this study to calculate the evolution of the solid fraction during the cooling stage since it is more adapted to a high cooling rate. The Scheil-Gulliver approximation assumes the equilibrium at the interface between liquid and solid, an infinite diffusion coefficient in liquid, and no diffusion in solid. Figure 1 illustrates the calculation of $\Delta T$ for the three reference alloys, where the solidification path was calculated using the ThermoCalc software with TCAL2 database. The calculation was run using TC-Python API, and $\Delta T$ was simply calculated from the model output as the difference of temperature between the lower and upper solid fraction limits.

### 2.3 Controlling the phases fraction

Most commercial aluminum alloys are constituted of a FCC $\alpha$ aluminum matrix with secondary phases. The high ductility of aluminum alloys results from the FCC $\alpha$ phase, with a large number of slip systems promoting plasticity. Secondary phases have several distinct contributions to the properties of the alloy. First it can result in precipitation hardening to increase the yield stress [29]. However, an increase of intermetallic precipitation results in a dramatic decrease of ductility. For instance, the yield stress of 7XXX alloys is about ten times higher than pure aluminum, but it comes with an elongation also ten times lower. If precipitation becomes uncontrolled and reaches unusual values, elongation at fracture may reach undesirably low levels. Secondary phases may also be formed for other purposes, such as controlling the chemical composition of phases, or modifying their morphology.

The total fraction of FCC phase was calculated at the equilibrium ($f_{FCC}$) at a constant temperature representative of a typical aging treatment. A single-point equilibrium calculation with Thermo-Calc and TC-Python API was used. Since the nature of the designed alloy is not known before simulations, the equilibrium temperature to select for a possible aging treatment remains unknown at this stage. Therefore the selection of the equilibrium temperature can only rely on empirical knowledge. The input alloying elements were conscientiously chosen, as developed in section 3.2, and the designed alloy would in all probability belong to 6XXX or 7XXX series (Al-Mg-Zn-Si). Zander [30] proposed to use equilibrium temperatures for Thermo-Calc calculations between 200°C and 500°C for those series, depending on the simulated heat treatment and the grade. In addition, the precipitation kinetics of secondary phases is maximal between 300°C and 400°C for most of the 6XXX and 7XXX alloys according to TTT diagrams [31]. Hence, it is proposed to use in the present paper the average equilibrium temperature of 350°C to launch the design alloy optimization process.

Of course, in no case, the computed FCC fraction should be considered as a realistic estimation after LPBF followed by aging, because the effective thermal path during LPBF is severely anisotherm, and because different aging temperatures may be selected. The computed FCC fraction at 350°C simply acts as a filter to preserve a sufficient - but not excessive - precipitation at this temperature during a potential ageing treatment, in comparison with usual commercial alloys. The total fraction of FCC phase at 350°C, $f_{FCC}$, will be then controlled during the optimisation process (considered as a constraint).

Figure 2a presents the fraction of FCC phase at 350°C for the reference alloys. It can be observed that for all alloys, the FCC phase fractions is lying between 88 % and 94 %. Hence, as a constraint, we impose that the total fraction of the FCC phase, $f_{\mathrm{FCC}}$, has to be lower than $f_{\mathrm{FCC,max}} = 0.94$, so that precipitation would remain possible in a similar way as in reference alloys, with at least the same $f_{\mathrm{FCC}}$ as in 6061 grade. In addition, we impose $f_{\mathrm{FCC}}$ to be larger than 70% to prevent the excessive formation of secondary phases that would be detrimental for the properties of the alloy: such a high fraction of

secondary phases is not met for commercial alloys, and it would very likely result in poor mechanical properties.

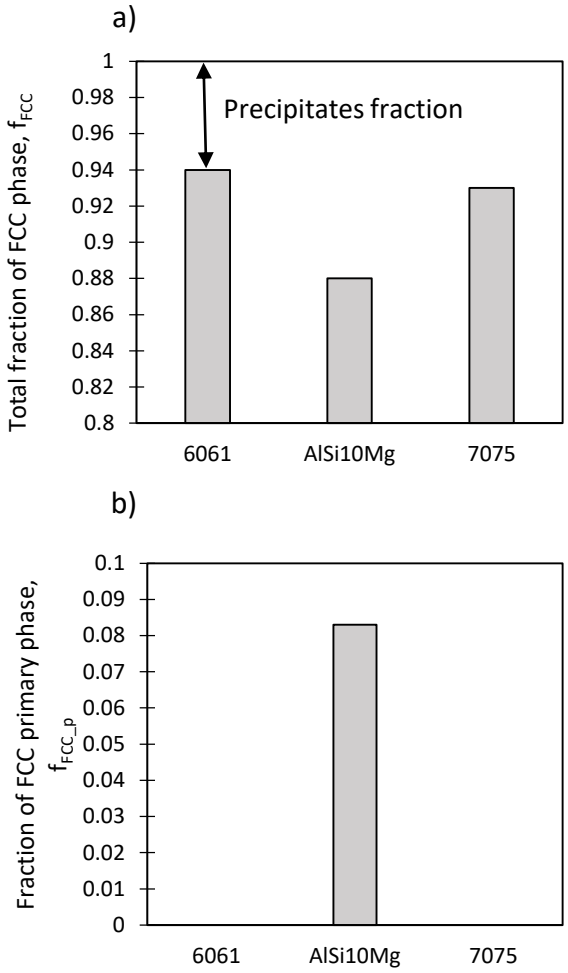


Figure 2: a) Evaluation of the total fraction of the Al-FCC phase for 6061, AlSi10Mg, and 7075 at 350°C; b) evaluation of the Al-FCC primary phase for the three alloys. Fractions are calculated by the CALPHAD method (ThermoCalc 2020b, TCAL2)

An additional criterion is proposed to penalize the formation of initial primary intermetallic phases during the solidification. This penalty is justified for two reasons. First, intermetallics have frequently a low crystalline symmetry and they form very sharp crystalline structures such as needles or plates, often very brittle. If they form first, large brittle phases will grow first, followed by ductile FCC. Such a structure is not expected to promote high mechanical properties [32] or thermal strain accommodation in the mushy zone. Instead, it is preferable to form first FCC grains ensuring ductility and then fine intermetallics. The formation of fine interdendritic phases was found beneficial to reduce hot cracking by preventing the formation of a continuous liquid film and by dendritic bridging [33]. A second reason is to prevent the absorption of the solute elements in primary intermetallics that would reduce the chance to entrap solute elements in FCC phase, needed in solid solution strengthening. This criterion is confirmed, at least partially, by Figure 2b showing that only AlSi10Mg first solidifies in Al-FCC phase (8 %). Therefore, the presence of FCC primary phase may contribute to the good weldability of this alloy. Hence, the fraction of FCC primary phase, $f_{\mathrm{FCC\_p}}$ calculated from Scheil model will be considered as an objective to increase. To calculate this fraction, a Scheil solidification calculation is

run with Thermo-Calc, with the help of TC-Python API. The software returns the phases names and the temperature, as a function of the solid fraction. When solidification starts with FCC phase, $f_{\mathrm{FCC\_p}}$ is calculated from the model output as the maximal value of the solid fraction where FCC is the only phase to be formed. Otherwise if solidification starts with a different phase, $f_{\mathrm{FCC\_p}}$ is set to zero.

### 2.4 Strengthening

There are three different hardening mechanisms in aluminum alloys contributing to the desired mechanical properties. They can be expressed in terms of the yield stress $\sigma_y$ as follows [29]:

$$\sigma_{\mathrm{y}} = \sigma_0 + \Delta\sigma_{\mathrm{ss}} + \Delta\sigma_{\mathrm{p}} + \Delta\sigma_{\mathrm{g}} \qquad (2)$$

with $\sigma_0$ the yield stress of pure aluminum single-crystal, $\Delta\sigma_{ss}$ the solid-solution contribution, $\Delta\sigma_p$ the precipitation contribution, and $\Delta\sigma_g$ the Hall-Petch grain size effect. For non-hardenable aluminum alloys (1XXX, 3XXX, 5XXX), most of the strengthening comes from solid solution hardening [34,35] whereas for hardenable alloys (2XXX, 6XXX, 7XXX) it mainly comes from precipitation hardening and solid solution [30,36].

The contributions of $\Delta\sigma_p$ and $\Delta\sigma_g$ are severely dependent on both the thermal field of the LPBF process and eventual post-processing annealing. In a first approach, considering the predisposition of aluminum alloys for precipitation, one may consider that precipitation hardening will probably remain possible for most of the selected alloys. Small compositional adjustments or smart aging treatments could provide sufficient hardening [37]. Therefore, a specific emphasis will be dedicated to the increase of $\Delta\sigma_{ss}$, since this term increases the yield stress with a low risk of embrittlement and properly penalizes the dilute alloys.

Solid solution hardening comes from the interaction between the strain field created by solute atoms and the moving dislocations. The strain field results from the mismatch in size and modulus of the solute atoms [38] :

$$\begin{aligned} \epsilon_{\mathrm{b}} &= \frac{\mathrm{d}b}{b\mathrm{d}c} \\ \epsilon_{\mathrm{S}} &= \frac{\mathrm{d}\Omega}{\Omega\mathrm{d}c} \\ \epsilon_{G} &= \frac{\mathrm{d}G}{G\mathrm{d}c} \end{aligned} \qquad (3)$$

where $\epsilon_{\mathrm{b}}$, $\epsilon_{\mathrm{S}}$ are related to the atomic radius misfit and $\epsilon_{\mathrm{G}}$ is related to the elastic bulk modulus misfit, $b$ is the Burger vector, $\Omega$ the atomic volume, $G$ the shear modulus, $c$ the atomic fraction of the solute. A combined mismatch $\epsilon_{\mathrm{L}}$ parameter can be introduced to describe the solid solution hardening effect:

$$\epsilon_{\mathrm{L}} = \sqrt{(\epsilon'_{\mathrm{G}})^2 + (\alpha\epsilon_{\mathrm{b}})^2} \qquad (4)$$

with $\epsilon'_{\mathrm{G}} = \frac{\epsilon_{\mathrm{G}}}{1+0.5|\epsilon_{\mathrm{G}}|}$. The solid solution strengthening contribution of a solute element j to the yield stress can be expressed by the following equation [34,39]:

$$\Delta\sigma_{\mathrm{SSH}} = K\epsilon_{\mathrm{L,j}}^{4/3} c_{\mathrm{j}}^{2/3} \quad (5)$$

with *K* a constant. Zander [30,34] showed that the size misfit effect is dominant compared to the dislocation-solution interaction in the specific case of aluminum alloys. Based on this assumption, the modulus misfit will be neglected when proposing an optimizing objective for a solid solution. Therefore, the size misfit contribution $\epsilon_{\mathrm{b}}$ alone was considered in this work. The magnitude of Burgers vector is $b = \frac{a}{2}\sqrt{h^2 + k^2 + l^2}$ for a FCC crystal with a lattice parameter *a*. For FCC lattices, dislocations move in the dense direction <110> so that $h = k = 1$ and $l = 0$, then, $b = a\sqrt{2}/2$. In addition, the lattice parameter can be expressed as a function of an equivalent atomic radius *r*: $a = \frac{4r}{\sqrt{2}}$. Finally, the size misfit contribution $\epsilon_b$ becomes:

$$\epsilon_{\mathrm{b}} = \frac{\mathrm{d}r}{r\mathrm{d}c} \quad (6)$$

For concentrated solid solutions, the determination of the lattice parameter *a* or the equivalent atomic radius *r* is not straightforward. Recent works of Toda-Caraballo et al. investigated the solution hardening for high entropy alloys [40,41], with an estimation of the lattice parameter by the approach of Lubarda [42] or by estimation of the interatomic distances [43,44]. In the current work, a quick estimation of the solid solution effect is sufficient, and the lattice parameter will be estimated with Vegard's law for the sake of simplicity. According to Vegard's law, the lattice parameter of a solid solution can be approximated by the weighted mean of the lattice parameter of its separated constituents. Consequently, for a binary alloy Al-Z the equivalent atomic radius r of the solution follows a weighted mean as well:

$$r = (1 - c)r_{\mathrm{Al}} + c \cdot r_{\mathrm{Z}} \quad (7)$$

With $r_{\mathrm{Z}}$ the atomic radius of the solute Z and $r_{\mathrm{Al}}$ the atomic radius of aluminum solvent. Eq. (7) implies that:

$$\frac{\mathrm{d}r}{\mathrm{d}c} = -r_{\mathrm{Al}} + r_{\mathrm{Z}} \quad (8)$$

Then by combining Eqs. (6), (7), and (8) :

$$\epsilon_{\mathrm{b}} = \frac{r_{\mathrm{z}} - r_{\mathrm{Al}}}{(1 - c)r_{\mathrm{Al}} + c \cdot r_{\mathrm{z}}} \quad (9)$$

Eq. 9 can be used to assess the capability of a solute element to increase yield stress by solid solution strengthening. However, this may not always result in a benefit for mechanical engineering if the strengthening occurs at the expense of density. Aluminum alloys have a low density that must be preserved, and strengthening is considered as a benefit for structural applications only if the specific strength $\frac{\sigma_{\mathrm{y}}}{\rho}$ increases [45]. Finally, to maximize the effect of solid solution for an element Z, it is

proposed to maximize the ratio $\frac{\Delta\sigma_{\mathrm{SSH}}}{\rho}$, with $\rho$ the density of the crystal determined by Vegard's law. According to Eqs. (5) to (9), this ratio becomes:

$$\frac{\Delta\sigma_{\mathrm{SSH}}}{\rho} = \frac{K \cdot N_{\mathrm{A}} \cdot 4\sqrt{2} \cdot c^{\frac{2}{3}}(r_{\mathrm{Z}} - r_{\mathrm{Al}})^{\frac{4}{3}}[(1-c)r_{\mathrm{Al}} + cr_{\mathrm{Z}}]^{\frac{5}{3}}}{(1-c)M_{\mathrm{Al}} + cM_{\mathrm{Z}}} \tag{10}$$

with *c* the solute concentration, $M_{\mathrm{Z}}$ the molar mass of the element Z and $N_A$ the Avogadro number. Eq. (10) quantifies the contribution of a given element Z in the FCC aluminum phase. By neglecting higher-order interactions, the contribution of all the alloying elements is then the sum of Eq. (10) over all the solutes, and it will be noted $I_{\mathrm{SS}}$ :

$$I_{\mathrm{SS}} = \sum_i \frac{c_i^{\frac{2}{3}}(r_{\mathrm{Z},i} - r_{\mathrm{Al}})^{\frac{4}{3}}[(1-c_i)r_{\mathrm{Al}} + cr_{\mathrm{Z},i}]^{\frac{5}{3}}}{(1-c_i)M_{\mathrm{Al}} + cM_{\mathrm{Z},i}} \tag{11}$$

where $i$ represents the index for the alloying element among the solutes population, and $c_i$ is the concentration of this element. Assuming a binary Al-Z alloy, Figure 3a shows the evolution of the solid solution index $I_{\mathrm{SS}}$ as a function of the alloying element content for Z={Mg, Zn, Fe, Si}. It is well observed that magnesium and zinc have the highest capabilities to strengthen the alloy by solid solution whereas silicon and iron present poor solubility in the aluminum FCC phase.

The solid solution index (Eq. 11) is also applied for the conventional alloys 6061, 7075, and AlSi10Mg, as presented in Figure 3b. 6061 and 7075 present the higher index compared to AlSi10Mg due to the high content of Mg and Zn (Table 1). Hence, one of the design rules would be to promote a solid solution index $I_{\mathrm{SS}}$ as high as possible.

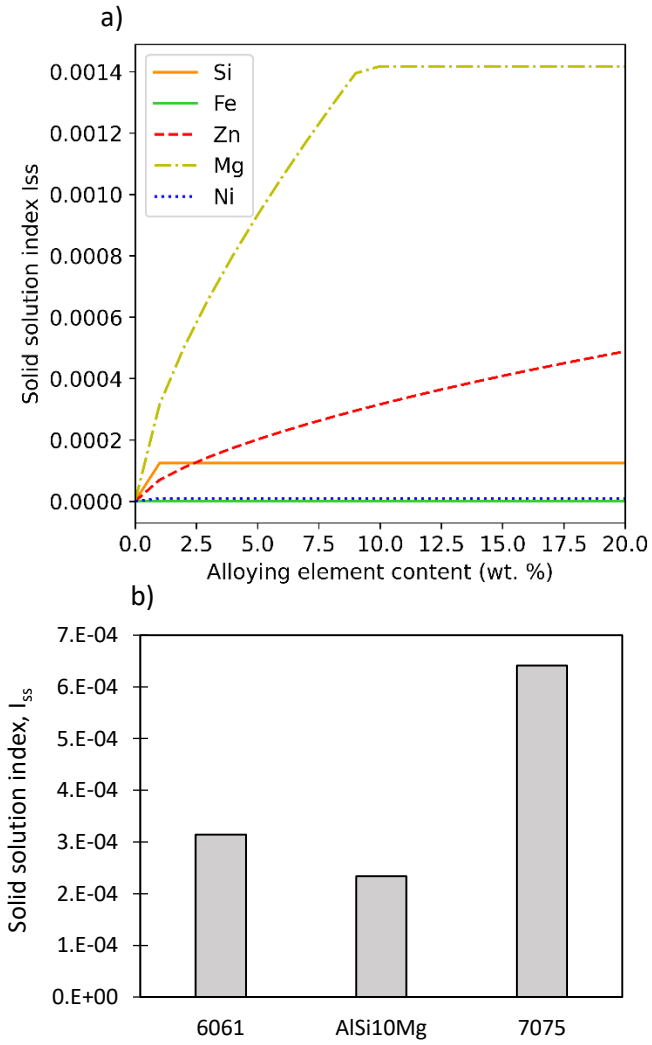


Figure 3: a) Evolution of the solid solution index $I_{SS}$ for different binary alloys Al-X (X = Mg, Zn, Fe, Si); b) calculation of the solid solution index for the three reference alloys 6061, 7075, and AlSi10Mg

## 3. Design of aluminum alloy

### 3.1 Genetic algorithm

An aggregated multi-objective genetic algorithm is used in this research work. Each alloy composition represents an individual with genes associated with the alloying element content (in weight %). The algorithm is described in Figure 4. First, a population of $n = 100$ individuals (generation 0) is randomly created. The whole population is evaluated and a fitness score $F$ is attributed to each individual. The fitness score is calculated by considering the objectives and constraints applied to the population. The population is ranked using the fitness score: the lower the fitness score the better the individual. Then, some individuals are selected into the population to make children either by elitism (the first 20 % of best individuals are selected) or by chance (some remaining individuals are selected with a probability of 0.05). The selected parents are randomly associated to create children. The cross-over method is used and consists to randomly swipe some pieces of genes from the parents to create children. Some children can mutate (10 % of chance), which means that randomly selected genes are assigned with a

random value. Then, the next generation is composed of the parents and their children ($n$ individuals). The algorithm continues until $N$ generations ($N = 50$) are created.

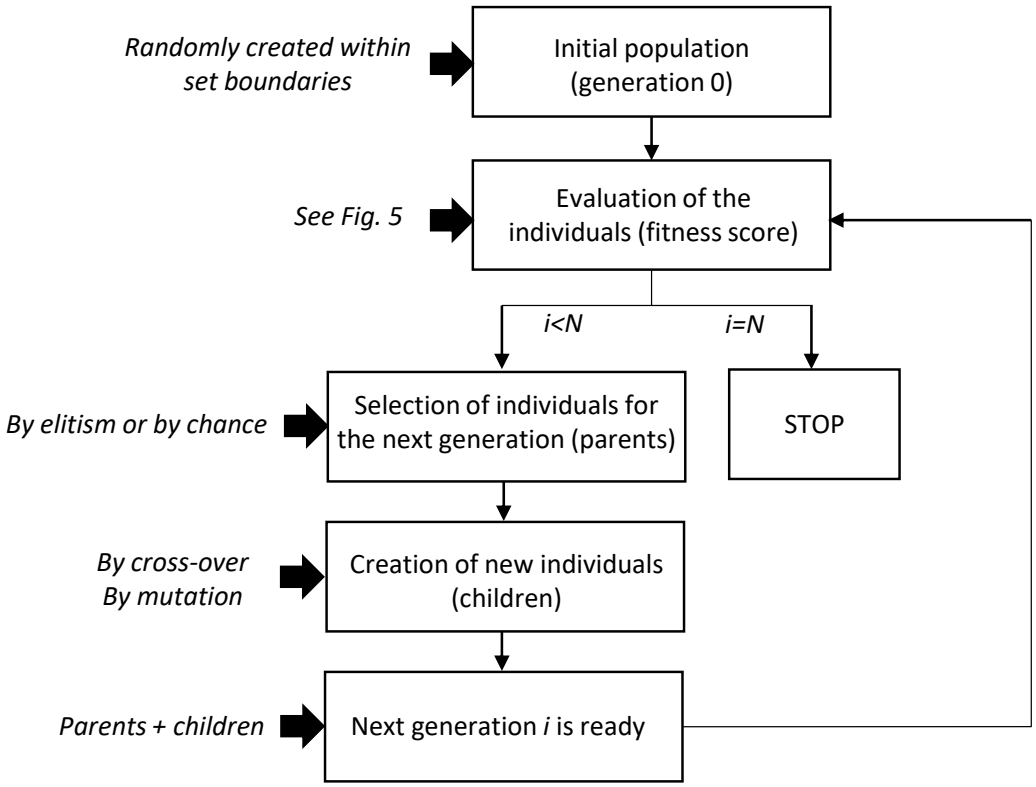


Figure 4: Genetic algorithm for alloy design

The main part of the algorithm is the calculation of the fitness score, based on the considerations detailed in previous section. Two constraints and two objectives are qualitatively set:

- The total fraction of FCC phase, $f_{\mathrm{FCC}}$, has to be higher than 0.7 and lower than 0.94 (constraint);
- The designed alloy has to first develop FCC primary phase during the solidification process to ensure ductility so that $f_{\mathrm{FCC\_p}} > 0$ (constraint);
- The solidification temperature range $\Delta T$ has to be as low as possible (objective);
- The solid solution index $I_{\mathrm{SS}}$ has to be as high as possible (objective).

Figure 5 details the evaluation process and shows how these objectives and constraints are implemented in the genetic algorithm. For each individual, a single point equilibrium calculation at 350°C is first done to obtain the concentration of each alloying elements in the FCC solid solution ($c_i$), and the fraction of the FCC phase ($f_{\mathrm{FCC}}$). Then, a Scheil-Gulliver calculation is made to obtain the fraction of FCC primary ($f_{\mathrm{FCC\_p}}$) and the solidification temperature range $\Delta T$. Finally, the solid solution $I_{\mathrm{ss}}$ index is calculated. If all the constraints are respected, the fitness score is calculated. Otherwise, a bad fitness score is assigned to the individual.

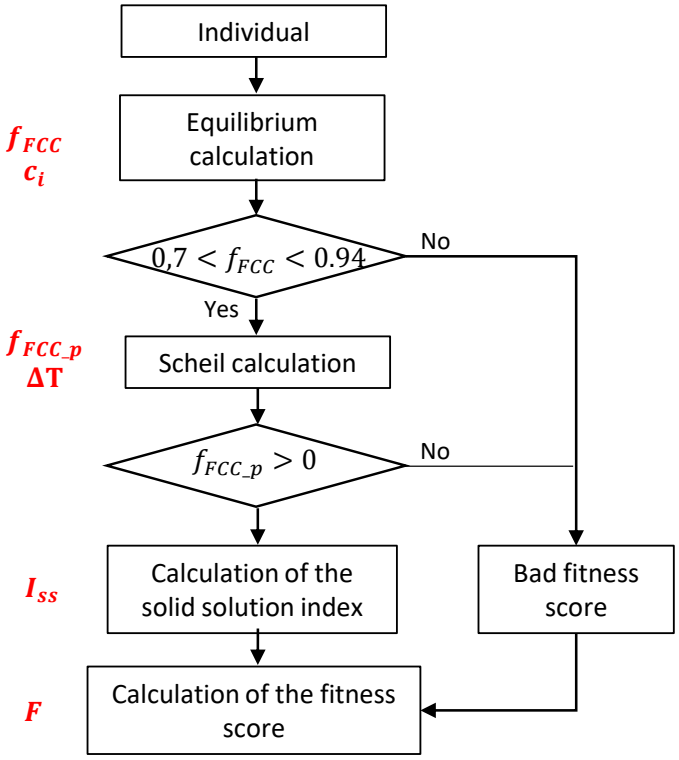


Figure 5: Thermodynamic calculations for the optimization process

The fitness score is defined as proposed in Eq. (12), where $\omega_{dt}$, $\omega_{\mathrm{FCC\_p}}$ and $\omega_{I_{\mathrm{SS}}}$ are some weights to adjust.

$$F = \omega_{dt} * \frac{\Delta T}{\Delta T_{\mathrm{ref}}} + \omega_{\mathrm{FCC\_p}} * \frac{1 - f_{\mathrm{FCC\_p}}}{1 - f_{\mathrm{FCC\_p,ref}}} + \omega_{I_{\mathrm{SS}}} * \frac{I_{\mathrm{SS,ref}}}{I_{\mathrm{SS}}} \qquad (12)$$

The weights were set with the values $\omega_{dt} = 0.4$, $\omega_{\mathrm{FCC\_p}} = 0.3$ and $\omega_{I_{\mathrm{SS}}} = 0.3$: the weight for $\Delta T$ is set to a higher value, because the main goal of the optimization is before all to select an alloy composition insensitive to hot cracking. To obtain a unitless fitness score, all the objectives are normalized by a reference value. For $\Delta T$ and $\mathrm{f_{FCC_p}}$, the reference value is taken for AlSi10Mg alloy because of its suitable resistance to hot cracking. For $\mathrm{I_{SS}}$ , the reference value is taken for 7075 alloy due to its resulting high strength. Values are: $\Delta T_{\mathrm{ref}} = \Delta T(\mathrm{AlSi10Mg}) = 12.6°\mathrm{C}$ ; $\mathrm{f_{FCC_p,ref}} = f_{\mathrm{FCC_p}}(\mathrm{AlSi10Mg}) = 0.08$ ; $\mathrm{I_{SS,ref}} = I_{\mathrm{SS}}(7075) = 0.00064$.

### 3.2 Input alloying elements

As an input of the optimization process, five alloying elements are selected: Si, Fe, Mg, Zn, and Ni.

- Silicon is chosen to decrease the brittle temperature range and then, to increase the weldability;
- Iron, in less quantity, may also influence the weldability of the alloy [46] and some authors showed that it can improve the mechanical properties of cast-alloy (Al-Mg-Si) [36];
- Nickel also influences the weldability of the alloy, as well as the mechanical properties by increasing the UTS due to the formation of homogeneous distributed submicrometric $Al_3Ni$ particles [47] or $Al_9FeNi$ [32,48].

- Magnesium is chosen since it promotes the formation of $Mg_2Si$ responsible for the strengthening of the alloy. Moreover, magnesium has a high solubility in the aluminum matrix, resulting in a valuable solid solution strengthening ([36] and Figure 3a);
- Finally, zinc is added to the initial composition to improve strength [13] and for its capacity to well dissolve in the matrix ([30] and Figure 3a). Age hardening of Al-Zn-Mg alloys may also form $MgZn_2$ particles, responsible for the hardening effect [30].

All the alloying elements can vary between 0 and 10 wt.% with an increment step of 0.01. If the content is lower than 0.01 %, the algorithm sets the value to 0.

### 3.3 Optimized alloy

After the optimisation procedure, a composition is selected, validating all the objectives and constraints. The optimised composition is : Fe = 0.3 wt. % ; Zn = 0.5 wt. %, Mg = 6.7 wt. %, Si = 3.0 wt. %, Ni = 1.4 wt. %.

This designed alloy (named "OA_1" for "Optimized Alloy n°1") presents all the required specifications, with a total fraction of Al-FCC phase equal to 0.87 and a fraction of FCC primary phase equal to 0.29 (Figure 6a and b). The fraction of precipitates is then equal to 0.13, possibly allowing precipitation hardening. The brittle temperature range $\Delta T$ is lower than the one of AlSi10Mg and equals 6°C, as shown in Figure 6c. Finally, Figure 6d shows that the solid solution index $I_{SS} = 0.00052$ is close to the one of 7075, and the possible solid solution strengthening is expected to be high.

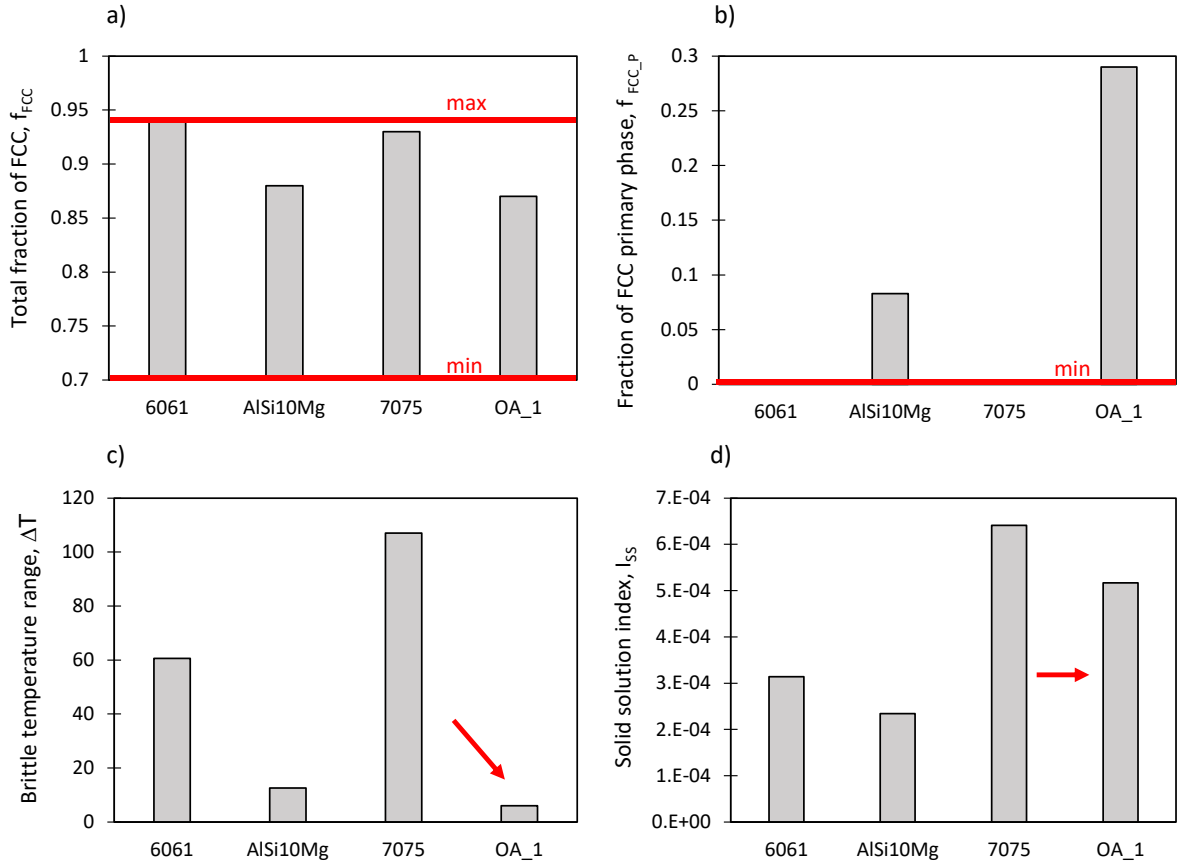


Figure 6: Comparison of the performance of the designed alloy "OA_1" to the three reference alloys AlSi10Mg, 6061, and 7075

Due to the ability of zinc to vaporize, it is proposed to increase its content to compensate for its loss during melting. The selective vaporization of elements might be calculated from Langmuir equation [49], however the vaporization flux depends severely on the melt pool temperature, which is not known properly at this stage. Therefore, the Zn fraction was increased to its maximal content to prevent any possible loss, while preserving the initial microstructure and performances of OA_1 alloy. According to the pseudo-binary diagram proposed in Figure 7, the phases met in OA_1 alloy remain the same for the temperature range of 300°C – 400°C considered for a possible ageing treatment, as long as the Zn fraction remains below 1 wt.%. Above 2 wt.%, the formation of T-phase ($(Mg)_{26}(Al,Mg)_6(Al,Mg,Zn)_{48}(Al)_1$) may occur during ageing, and the microstructure may differ. Therefore, the zinc content was increased to 1 wt.% to preserve from the formation of T-phase.

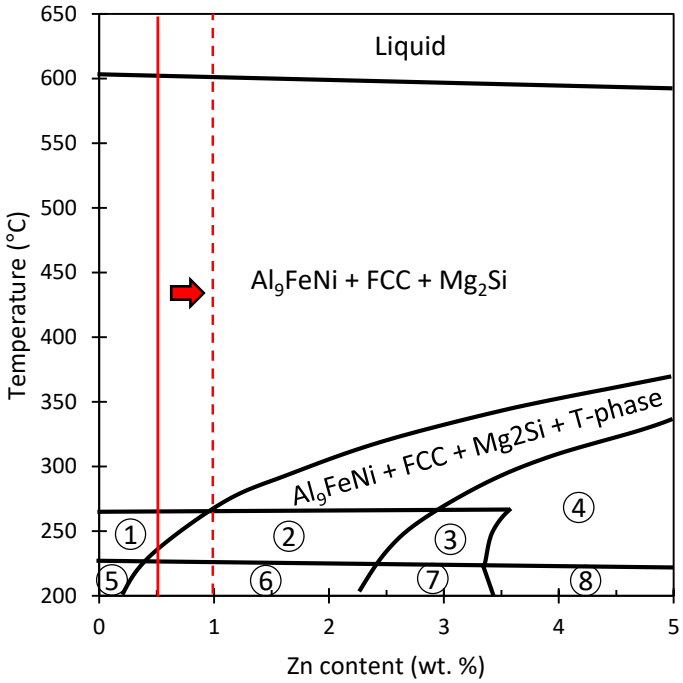


① $Al_{10}Fe_3Ni + Al_9FeNi + FCC + Mg2Si$
② $Al_{10}Fe_3Ni + Al_9FeNi + FCC + Mg2Si + T\text{-}phase$
③ $Al_9FeNi + Al_{10}Fe_3Ni + FCC + Mg2Si + C14\text{-}leave + T\text{-}phase$
④ $Al_9FeNi + FCC + Mg2Si + C14\text{-}leave$
⑤ $Al_{10}Fe_3Ni + Al_{13}Fe4 + FCC + Mg_2Si$
⑥ $Al_{10}Fe_3Ni + Al_{13}Fe4 + FCC + Mg_2Si + T\text{-}phase$
⑦ $Al_{10}Fe_3Ni + Al_{13}Fe4 + FCC + Mg_2Si + T\text{-}phase + C14\text{-}leave$
⑧ $Al_{10}Fe_3Ni + Al_{13}Fe_4 + FCC + Mg_2Si + C14\text{-}leave$

Figure 7: Equilibrium phase diagram of Al-Fe0.3-Mg6.7-Si3-Ni1.4-Znx

The retained composition for the optimized alloy is: Fe = 0.3 wt. %, Zn = 1 wt. %, Mg = 6.7 wt. %, Si = 3.0 wt. %, Ni = 1.4 wt. % (named "OA_2"). The FCC phase fractions, the brittle temperature range, and the solid solution index of OA_2 are almost the same as that of OA_1 ($f_{\mathrm{FCC}} = 0.87$, $f_{FCC\_p} = 0.28$, $\Delta T = 9°C$, $I_{\mathrm{SS}} = 0.00055$).

Figure 8a shows the evolution of the different phase fraction of OA_2 alloy as a function of the temperature (at the equilibrium). For temperatures higher than 300°C, the stable phases are Al-FCC, $Al_9FeNi$, and $Mg_2Si$. At lower temperatures, other phases such as $Al_{10}Fe_3Ni$, T phase, or $Al_{13}Fe_4$ are formed at the expense of the FCC phase. However, the reliability of CALPHAD calculations at low temperature is limited. Moreover, the formation of these phases by diffusive solid-state transformation is unlikely during the rapid cooling step of LPBF process. Figure 8b illustrates the evolution of the temperature with respect to the solid fraction during solidification, according to Scheil model. The OA_2 alloy would start solidification by the formation of primary FCC in agreement with the criterion of section 1.4. Then the solidification pursues with the joint formation of $Mg_2Si$ and $Al_9FeNi$.

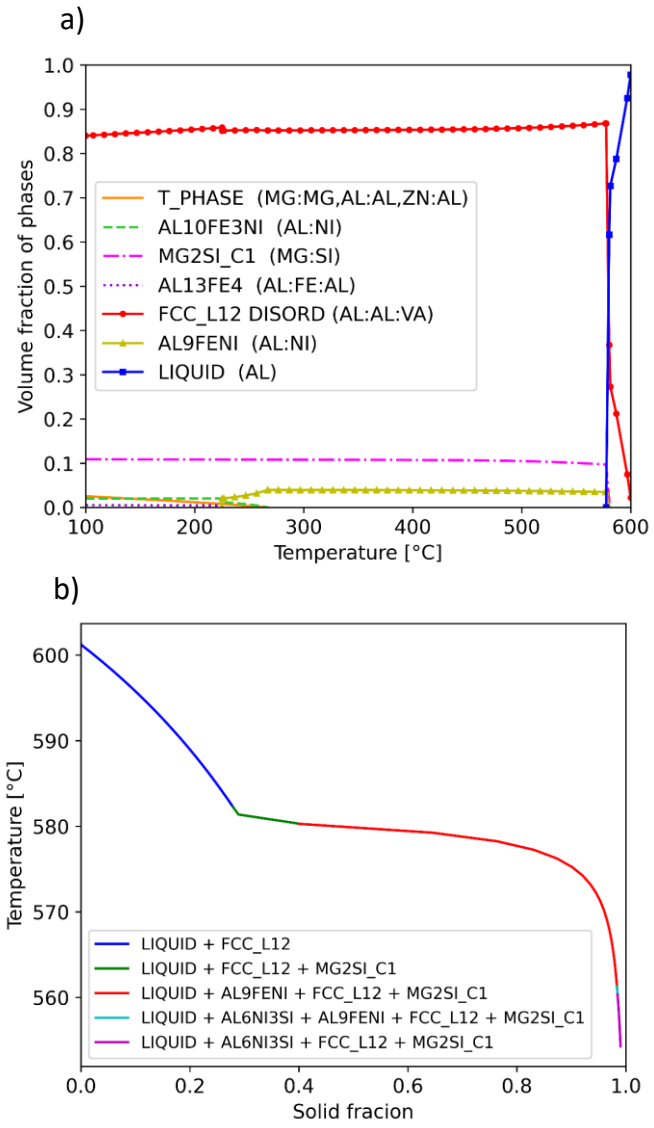


Figure 8: a) Evolution of the phases fractions of the alloy OA_2 as a function of the temperature; b) Sequence of formation of phases during solidification according to Scheil model

## 4. Experimental results

### 4.1 Experimental methods

#### 4.1.1 Microstructure and chemical analyses

The characterization of the built material was done by SEM on a JEOL 6500F FEG microscope at 20 kV. Electron Back-Scattered Diffraction (EBSD) mapping was conducted on a Zeiss Supra 55 VP microscope operating at 20 kV. The variations of chemical composition were characterized by a Back-Scattered Electron (BSE) detector and by Energy Dispersive X-Ray Spectrometry (EDX) mapping.

The identification of phases was achieved by X-Ray Diffraction (XRD) (X'Pert Pro Panalytical) using a Copper X-ray tube and divergence slits at 0.5° for the incident beam, and anti scatter slit at 0.5° with a graphite monochromator and a Miniprop point detector for the diffracted beam. The diffraction angle 2θ varied from 10° to 138° with a step size of 0.03°, and a counting time of 25 s/step.

#### 4.1.2 Powder production

The optimal alloy predicted by GA was externally produced by gas atomization by the company Ducal International (France). The target granulometry was set to +10 µm /-75 µm. Granulometry was measured by a laser granulometer (Malvern Mastersizer Hydro2000) with a gas pressure of 3.5 bars. The particle distribution is illustrated in Figure 9a, and it follows a log-normal distribution with parameters µ=4 µm, $\sigma$=0.36. This distribution corresponds to a mean size equal to 59 µm, a median size of 55 µm, and a standard deviation of 22 µm. The morphology is spherical with a low fraction of satellites or irregular particles, as shown in Figure 9b.

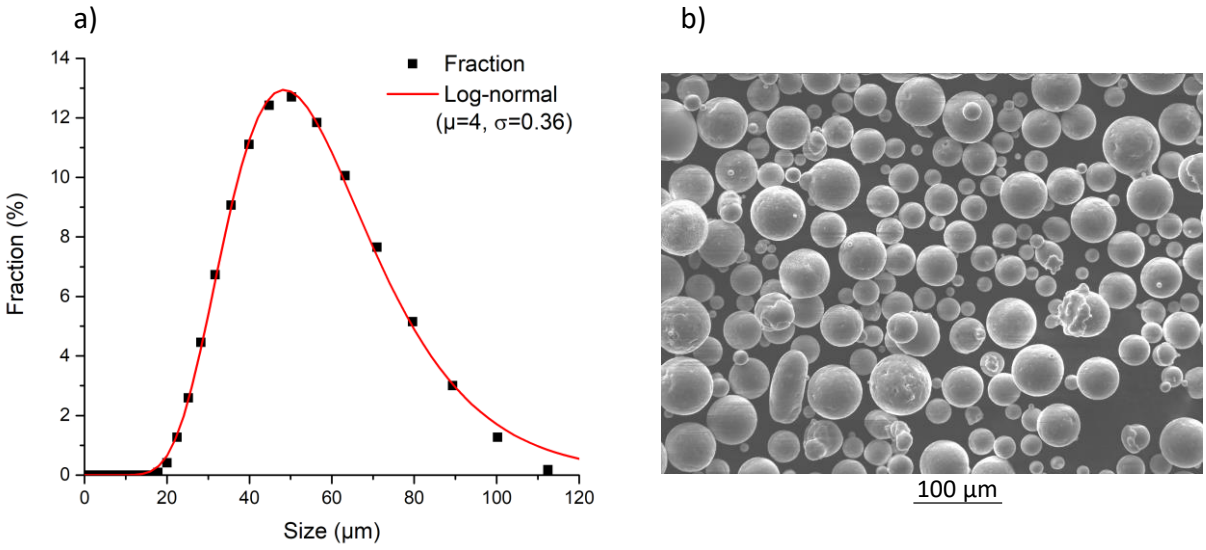


Figure 9: a) Particle size distribution (black dots) fitted by a log-normal distribution (red line), b) SEM image of the particles

#### 4.1.3 LPBF manufacturing

The powder was used in a ProX 200 PBF-LB machine from 3D Systems to fabricate square specimens with dimensions 8 x 8 x 3 mm, cube specimens with dimensions 10 x 10 x 10 mm, and rectangular specimens with dimensions 42x5x15 mm to observe eventual distorsions and to be used for tensile tests. On the build platform of 140 x 140 mm, specimen were disposed in the following way : three

rectangular specimen were placed on the left side of the build platform with their long side parallel to the platform and to the roller direction, three rectangular specimen were oriented normally to the build platform, and on the right side three cubes were built for microstructure analysis. Specimen were disposed in staggered rows , and the building sequence was also oriented in the opposite direction of the Ar gas flow, to prevent defects due to spatters ejection from neighbor parts. The building job was repeated twice to obtain a sufficient number of specimen for tensile tests, with no specific difference noted between the two jobs. No heating was applied to the build platform during the process. The laser source operates at near-infrared spectrum ($\lambda$=1064 nm), with a variable power $P$ in the range 200-300 W. The laser scanning speed was kept constant at v=1000 mm/s, the hatching distance was set at 70 µm, and the powder layer thickness was 40 µm. The scanning strategy selected was -45/+45° compared to the orthogonal axis of the square specimens.The tensile test specimens were cut from 42x5x15 $mm^3$ plates, following two orientations : one along the scanning direction (SD, parallel to the building platform) and one along the building direction (BD, normal to the building platform). Tensile test specimens had a reduced section with a square cross-section of 25 $mm^2$ and a length of 20 mm as illustrated in Figure 15. Surfaces were polished with sand paper until 1200 mesh to remove surface roughness that may affect the fracture initiation.

#### 4.1.4 Mechanical testing

Tensile tests were conducted on a Instron 1186 device with a speed of 10 µm/s, and the elongation was measured by a clip-on extensometer with an initial gage length of 10 mm. Tensile tests were repeated five times for each orientation, the average and the standard deviation of mechanical properties were determined. Macro-hardness tests were conducted with a Wolpert Testwell machine, with a load of 10 kg and a dwell time of 10 seconds.

### 4.2 Analysis of the microstructure after LPBF manufacturing

Several specimens were built with variable laser power, and the resulting structure is illustrated in Figure 10. For a power intensity of 200 W, a large amount of porosities (3 % in this image) is visible. These porosities have an irregular shape elongated orthogonally to the Building Direction (BD). This morphology corresponds to “lack of fusion” defects, indicating an inadequate overlapping of the seams. The porosity fraction significantly decreases when power is increased to 240W, and nearly no porosities are observed at 280 W. This confirms the origin of these porosities: increasing the power increases the seam size, and the overlapping becomes sufficient to prevent lacks of fusion. Additionally the surface quality turns out to be increased at 280 W (lower roughness), confirming the regularity of the tracks juxtaposition and the stability of fusion pools with these optimized conditions.

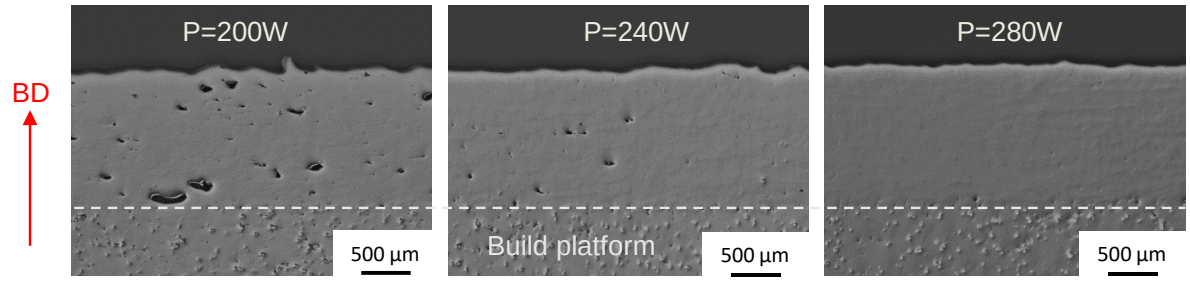


Figure 10: Optical observations of porosities in the build material for a variable laser power

After chemical etching with Keller reagent, the melt pools are observed by optical microscopy, and the result is illustrated in Figure 11a. The laser scanning direction is oriented horizontally, with a rotation of 90° between each layer. Therefore some elongated melt pools are observed in domain A, corresponding to a scanning direction along X-axis. In domain B, some melt pools are visible along their normal cross-section, corresponding to a scanning direction along Y-axis. The melt pool size is estimated to be 160 µm wide, and 150 µm in depth after measurements of the top layer. Figure 11b illustrates the microstructure at a higher magnification observed by SEM. One can observe the occurrence of porosities of 1 -5 µm diameter with a small aspect ratio (red arrows). These porosities could result from the vaporization of some volatile elements such as Mg. This is confirmed by the lower concentration of Mg in the LPBF material compared to the powder, as indicated in Figure 17 in the Complementary Results section.

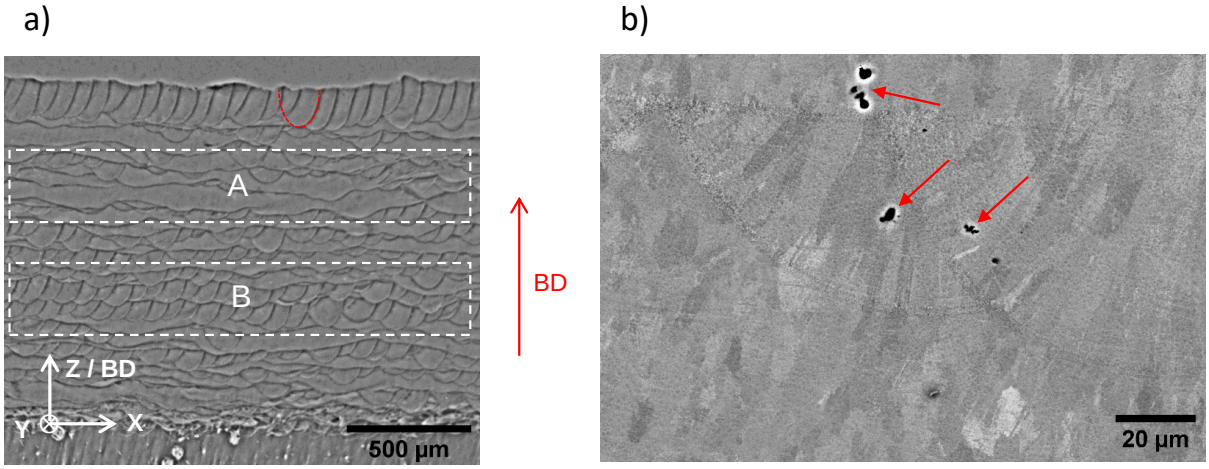


Figure 11: a) Observation of the melt pools for P=280 W by optical microscopy imaging after Keller etching, b) SEM observation of porosities on the same specimen at higher magnification

To determine the nature of phases, X-ray diffraction measurements were conducted, and the diffraction pattern is illustrated in Figure 12 for both the powder and for the LPBF bulk material. The patterns exhibit clearly defined peaks representative of FCC $\alpha$-Al with a lattice parameter a=4.05 Å, corresponding to the ICDD card n°01-072-3440. A secondary phase was identified as FCC $Mg_2Si$ phase with a lattice parameter a=6.34 Å (ICDD card n°04-001-9399). Finally, smaller peaks are observed between $2\theta$ = 20° and 50°, and after comparisons with the database PDF4+, the best candidate may be the phase $Al_9FeNi$, with a P21/c monoclinic structure (ICDD card n°04-024-7873). However, the peak intensity is very low; and there is still some uncertainty on the identification. Additional analyses are required to confirm the exact crystalline structure of this third phase. The phases identified are in good agreement with CALPHAD predictions (Figure 8), and it confirms the reliability of the thermodynamic calculations.

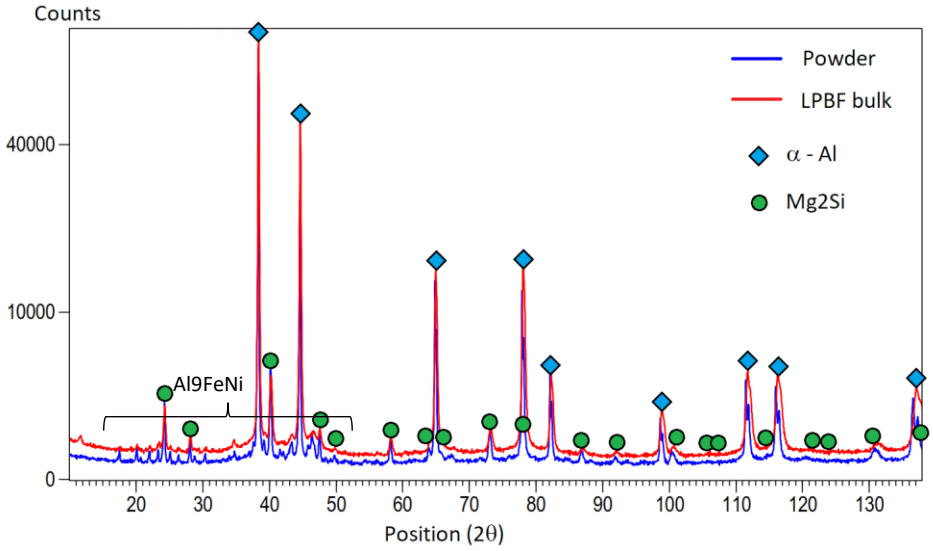


Figure 12: X-ray diffraction diagram of the powder (blue line) and the LPBF manufactured bulk specimen

The microstructure was further characterized by EBSD mapping, and the IPF Z (parallel to BD) orientations map is shown in Figure 13 for FCC $\alpha$-Al. Melt pool cross-sections can be identified by large domains with columnar grains (dashed lines, area B). This columnar structure is frequently met in aluminum alloys by LPBF [50]. The columnar grains are oriented radially toward the center of the melt pool, corresponding to a growth in the direction of the thermal gradient. The columnar grains have a length in the range 20–50 µm and a width between 3 and 10 µm.

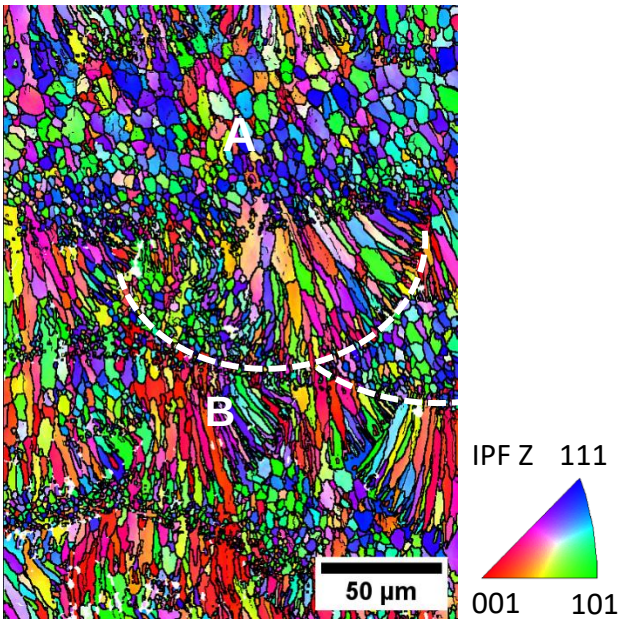


Figure 13: EBSD IPF map for P=280 W, revealing a columnar structure

Some other areas of the EBSD map are populated with apparently equiaxed grains (area A), and melt pools cross-sections are no more visible. This would correspond to seams with a scanning direction along the X-axis. The apparent equiaxial morphology may result from the 2D cut of columnar structures tilted according to the Z-axis and pointing in the direction of the thermal gradient.

Figure 14 illustrates BSE imaging of the melt pools section normally to the scanning direction. Different levels of gray are indicating some variations of chemical composition. At low magnification, one can observe the melt pool boundary (white dashed line in Figure 14a), and the large columnar grains oriented toward the pool center (blue dashed lines in Figure 14a). Imaging at higher resolution reveals a very fine structure constituted of globular dark gray grains with a size below 1 µm. These grains are surrounded by a secondary light gray phase (highlighted in blue in Figure 14b) and a third phase composed of dark dots (highlighted in red in Figure 14b). These two phases have a size below 100 nm, and by image analysis (using Python Scikit-Image) they represent 2% ($\pm$ 1%) for the light gray phase, and 8% ($\pm$ 2%) for the black phase. Therefore, FCC phase fraction is estimated around 90%.

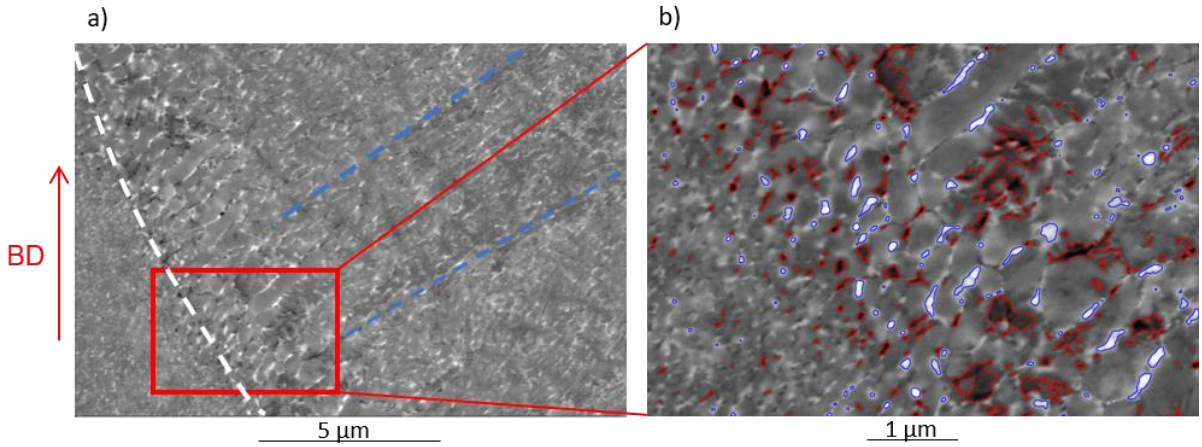


Figure 14: BSE SEM imaging for P=280 W, revealing the precipitation of phases in $\alpha$-Al

Globular gray grains are largely predominant, and they would obviously correspond to the FCC $\alpha$-Al. The light gray phase (highlighted in blue in Figure 14b) would correspond to a high concentration of elements with a large Z number, and therefore it would correspond to $Al_9FeNi$. The powder characterization performed by XRD presented in Figure 12 confirms the presence of $Al_9FeNi$ precipitates. The dark contrast features (highlighted in red in Figure 14b), associated to low Z atomic number would correspond to $Mg_2Si$. Once again, $Mg_2Si$ was clearly identified on the X-ray diffraction pattern presented in Figure 12. A more detailed work need to be done to confirm phase identification, which is not the scope of the present work.

### 4.3 Mechanical properties

Mechanical properties were evaluated by tensile tests (Figure 15a) along the building direction (BD, red line) and the scanning direction (SD, black line). Cross markers indicate the last point of the curve at failure. Table 3 indicates the average values of mechanical properties $\pm$ the standard deviation.

*Table 3: Mechanical properties of OA_2 obtained after tensile tests*

| | Yield stress (MPa) | Ultimate tensile strength (MPa) | Elongation at break(%) |
|---|---|---|---|
| Building direction | 431 ± 14 | 514 ± 25 | 1.1 ± 0.5 |
| Scanning direction | 416 ± 6 | 494 ± 61 | 1.7 ± 1.6 |

A higher strength is observed along BD, with an average yield stress (YS) of 431 MPa and an average ultimate tensile strength (UTS) of 514 MPa. These values are weakly scattered, with respective

standard deviations of 14 and 25 MPa. This high strength is associated with a brittle behavior: cracking occurs suddenly for elongation values as low as 1%.

Mechanical properties along the scanning direction are slightly different : both YS and UTS are 4% lower than for BD. This is associated with slightly larger ductility of the material, with a mean ultimate elongation (A%) of 1.7%, and a maximal value at 4.5%. However ultimate elongation values are significantly scattered, with a standard deviation of the same range as the mean value. Therefore there is a significant risk of fracture in the elastic domain, as it was observed for one specimen. Finally, the hardness of the material was measured by macro-indentation, with a value of 162 $HV_{10}$.

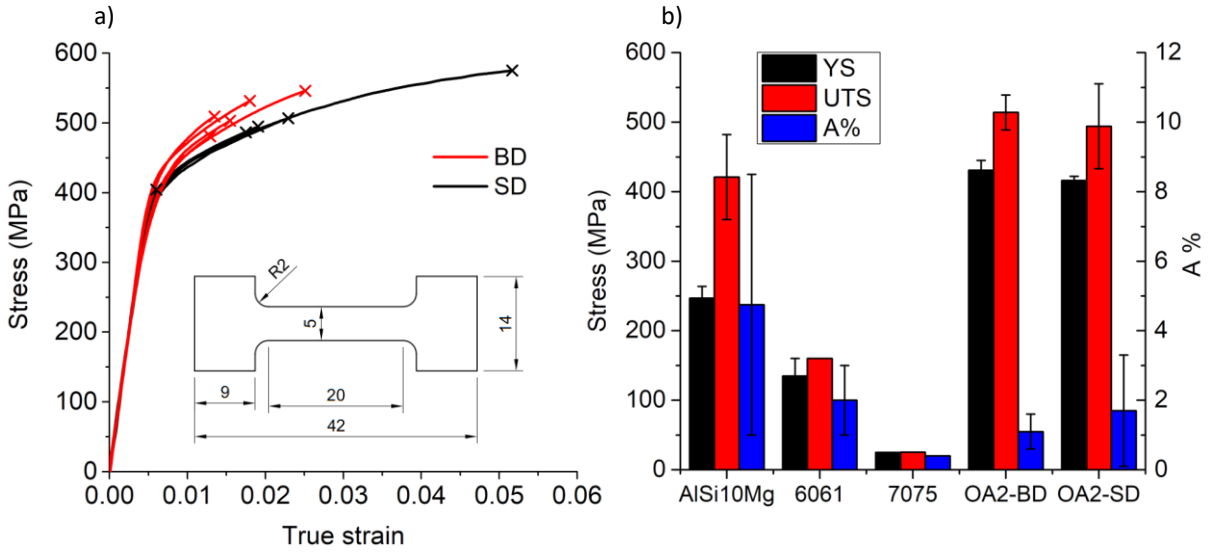


Figure 15: a) Tensile test curves for two different specimen orientations ; b) comparison of the mechanical properties to the reference alloys

Figure 15b illustrates a comparison of the mechanical properties of the reference alloys obtained by LPBF (data from Table 2) and OA_2 (data from Table 3). The error bars correspond to the amplitude of variation indicated on Table 2 and Table 3. OA_2 shows a YS and a UTS respectively 80% and 40% higher than for AlSi10Mg. The significantly higher mechanical strength compared to 6061 and 7075 are associated to the mitigation of hot cracking. Finally, the elongation at break is within the usual range for AM aluminium, with a low value of a few percents very comparable to 6061 and 7075.

To understand the reasons for the early failure and the very low ductility of the material, the fracture surface was observed for tensile tests along SD and BD (Figure 16). In Figure 16a, it can be noticed the occurrence of porosities along SD indicated by red arrows. These defects from the LPBF process may be the cause for the rapid initiation of damage. The fracture surface shows cleavage steps associated with intergranular fracture. This fracture mode is consistent with the brittle behavior of the material. The fracture surface for traction along BD is quite different, as illustrated in Figure 16b. The fracture occurred by decohesion between two successive layers of material, following the interface between seams. In addition, some particles and cavities are observed (indicated by red arrows) and correspond to the decohesion of secondary phases. The formation of coarse intermetallic phases at the junction between seams, as visible in Figure 14, is a possible explanation for the decohesion between the building layers.

a) SD

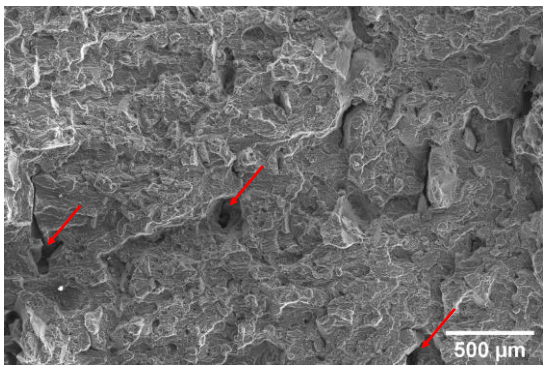


b) BD

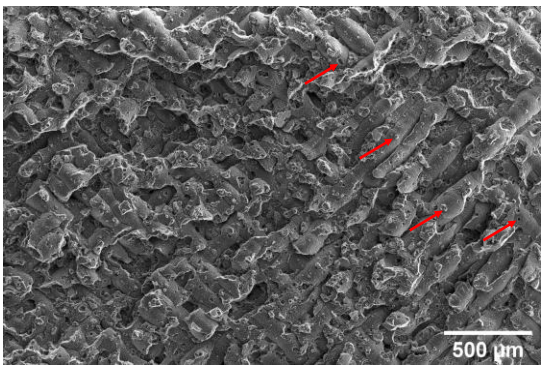


Figure 16: SEM imaging of the fracture surface for a tensile test a) along SD, and b) along BD

## 4.4 Discussion

New criteria for the design of a new aluminum alloy were formulated to decrease the risks of hot cracking and to enhance the mechanical properties. Several criteria have been proposed and will be now discussed in the light of the experimental results.

- **Hot-cracking mitigation**

In order to mitigate hot-cracking, a criterion was set to minimize the brittle temperature range $\Delta T$ computed based on the Scheil model. Figure 10 and Figure 11 confirm the absence of cracks in the samples built by LPBF.

- **Phases formation control**

Two criteria were proposed to prevent the uncontrolled formation of brittle phases during LPBF process :

- Formation of primary FCC phase during the solidification
- Controlled quantity of precipitates

From experimental works, it can be seen that the α-Al structure in LPBF specimens characterized by EBSD (Figure 13) corresponds to columnar structures of several tens of micrometers. However, BSE imaging (Figure 14) reveals globular structures below 1 µm. Therefore, it must be concluded that the different small globular α grains observed in Figure 14 have the same crystalline orientation and then belong to the same columnar grain. Then, the secondary phases may form at the same time than the columnar FCC α grains. This is well supported by the Scheil calculation of Figure 8b: secondary phases are expected to be formed jointly with the FCC phase. Hence, Scheil model seems to well predict the solidification sequence and especially the joint formation of FCC and secondary phases. This can be attributed to the very high cooling rates met in LPBF process, consistent with the hypothesis of no diffusion in the solid phase in Scheil model.

- **Mechanical properties**

The last criterion concerns the mechanical properties of the alloy, where the solid solution hardening were promote during the optimization process. The mechanical properties of the designed alloy showed a yield stress around 420 MPa. This high value is only partially attributed to solid solution strengthening. Indeed, precipitation hardening usually has an important

contribution on increasing mechanical properties [30]. In addition, the designed alloy exhibit low ductility (elongation at break around 1.5%). According to Figure 16, the low ductility may be associated to different factors. First, the occurrence of defects, such as porosities, initiate early damage. This first point could be mitigated by additional process parameters optimization. Second, the presence of secondary phases result in an interfacial decohesion between seams and cause embrittlement. Embrittlement by secondary phases is mostly composition dependent, and it should constitute a significant research axis for the development of future aluminium grades. Hence, future works will focus on the control of the precipitation to tailor the mechanical properties. Especially, the effect of subsequent ageing and over-ageing treatments on the mechanical properties is an important point to study further. Over-ageing seems the most possible treatment: precipitates have already a significant size of tens micrometers in the LPBF material, and their coalescence and growth is expected during heat treatment. Over-ageing could help to recover a higher ductility, however by losing in the same time some strength.

## Conclusion

New criteria for the design of a new aluminum alloy were formulated to decrease the risks of hot cracking and to enhance the mechanical properties. The brittle temperature range $\Delta T$ was computed based on the Scheil model and minimized to reduce the hot cracking susceptibility. The content of solute elements was increased to benefit from the solid solution effect. On the other hand, some criteria on the precipitation fraction were included to prevent the uncontrolled formation of brittle phases. These objective functions were assembled in an aggregated genetic algorithm to search for an optimal composition. A new grade was determined by this algorithm, with the composition Al-Mg 6.7 %, Si 3 %, Ni 1.4 %, Zn 1 %, and Fe 0.3 %. This new composition is supposed to provide similar solid solution strengthening and precipitation capabilities as 6XXX and 7XXX series, with a low $\Delta T$ comparable to AlSi10Mg. The alloy was manufactured, gas atomized, and used for LPBF tests. The powder showed a suitable application for the LPBF process, with no occurrence of cracks and a limited fraction of porosities once the process parameters were set. Therefore, the design criterion relying on $\Delta T$ is a valid and is an efficient approach to mitigate the hot cracking issue. The alloy is constituted of primary FCC $\alpha$-Al phase, with $Mg_2Si$ and $Al_9FeNi$ intermetallic phases. Depending on the cooling speed, the sequence of formation of these phases is different: it forms by interdendritic segregation in the powder, but the phases form simultaneously in the case of the LPBF process. The mechanical properties of this new alloy were determined after LPBF processing. The alloy had a high strength comparable to 7075 grade produced by conventional ways, however associated to a low ductility. This brittle behavior was associated with the occurrence of porosities, and to the formation of secondary phases resulting in a low cohesion between the seams. Future developments of the algorithm should consider additional features concerning the nature of the intermetallics formed after solidification, and the capability to dissolve or precipitate these phases upon annealing or aging treatments to optimize the mechanical properties. These additional objective functions will increase the relevance of the selected alloy but will also increase the complexity of the multi-objective algorithm. Significant effort is actually dedicated to this task.

## Acknowledgement

The authors gratefully acknowledge the excellent support of Nathalie Peillon for X-ray diffraction and Claire Roume for the mechanical tests.

The authors express their sincere gratitude to the German-French Academy for the Industry of the Future founded by the Institut Mines-Télécom (IMT) and the Technical University of Munich (TUM) for financially supporting the research on the presented topic within the research project ADAM.

## Data availability

The raw/processed data required to reproduce these findings cannot be shared at this time as the data also forms part of an ongoing study.

## Complementary Results

These complementary results expose the different characterization perfomed on the powder.

a) Chemical characterizations

The chemical composition was controlled by EDX on the surface of particles, and on the polished cross-section. The composition is evaluated by an average over 8 randomly selected points, and the concentration of alloying elements is illustrated in Figure 17. A standard deviation of the composition below 1 % was observed, and no significant variation of the chemical composition could be detected. In general, the concentration of alloying elements is close to the nominal concentration, however, an excess of Mg is observed. This is especially remarkable when the concentration is measured at the surface of the powder: the Mg excess reaches +4.6 % and may be attributed to the possible formation of some magnesium oxides at the surface. The concentration measured by EDX in the cross-section of particles is more representative of the effective composition, and the Mg excess is only +0.9 %. For the other elements, the composition error measured on the polished cross-section is below +/-0.2 %, lower than the EDX resolution range.

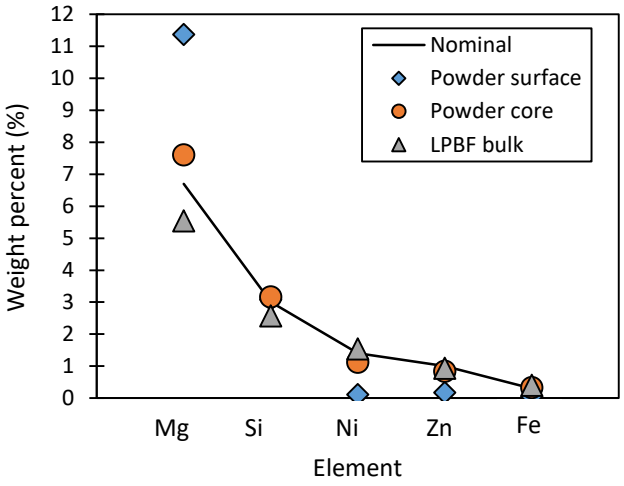


Figure 17: Comparison of the average concentration of alloying elements

b) Microstructure of the powder

Powder particles were observed by SEM, and their cross-section was observed using a backscattered electrons detector (BSE). In Figure 18a, we can observe large dendrite structures at the surface, representative of the solidification structure. On the cross-section (Figure 18b), three different levels of gray are visible by BSE inside the particle, revealing different domains of chemical compositions. The gray domains (A in Figure 18b) have the morphology of dendrites, and it corresponds to the primary growth of FCC $\alpha$-Al phase. Dark gray structures form jointly with the FCC phase, and it could correspond to $Mg_2Si$ phase, with a low brightness representative of lightweight elements. This is confirmed by EDX mapping (Figure 18c): B domains have a significantly higher Mg and Si fraction. This observation is in agreement with Scheil model (Figure 8): $Mg_2Si$ forms jointly with FCC from a solid fraction of 29%. It is also consistent with observations in the LPBF material (Figure 14). Light gray domains (C in Figure 18b) correspond to higher Z values, and they have the morphology of interdendritic phases. These domains are typically formed by the segregation of elements during the solidification and they concentrate all the heavier alloying elements, resulting in a higher brightness on the image. These structures have a size of a few micrometers, and it could correspond to the phase $Al_9FeNi$ formed at the end of solidification according to Scheil model on Figure 8. The identification of this phase is confirmed by the powder diffraction pattern illustrated in Figure 12. EDX mapping on Figure 18c reveals a higher fraction of Fe and Ni in these domains, confirming further the identification.

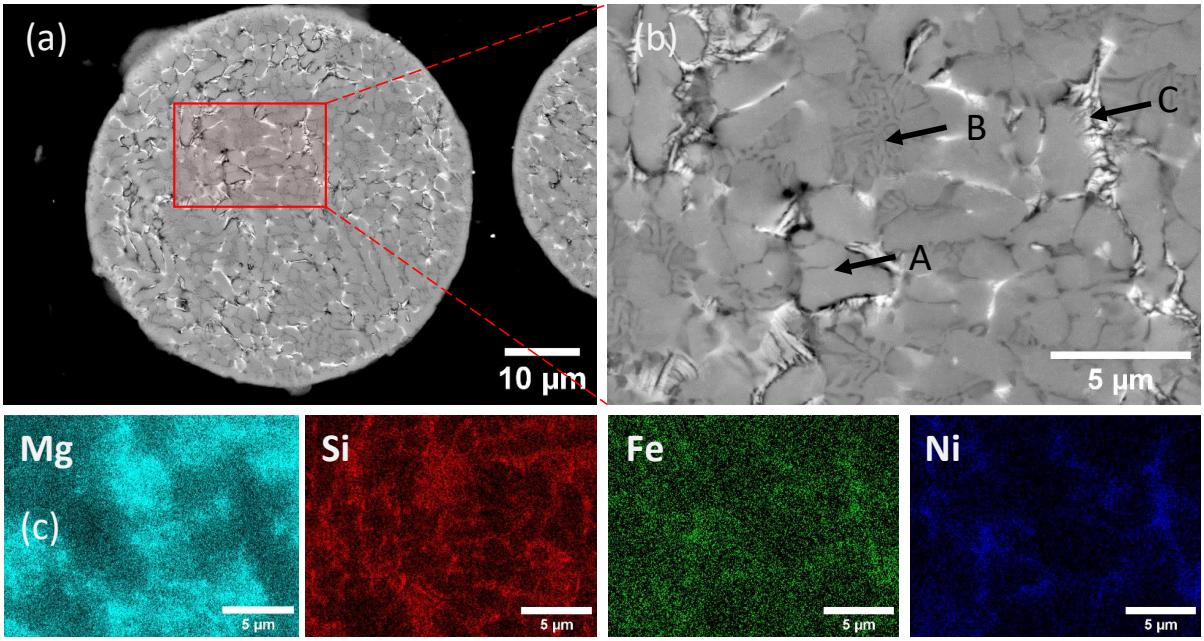


Figure 18: a) Secondary electrons imaging of the surface of a particle, b) BSE imaging of the cross-section, revealing primary dendrites and interdendritic phases, c) EDX mapping revealing the repartition of elements

## References


[1] E.O. Olakanmi, R.F. Cochrane, K.W. Dalgarno, A review on selective laser sintering/melting (SLS/SLM) of aluminium alloy powders: Processing, microstructure, and properties, Prog. Mater. Sci. (2015). https://doi.org/10.1016/j.pmatsci.2015.03.002.

[2] C. Galy, E. Le Guen, E. Lacoste, C. Arvieu, Main defects observed in aluminum alloy parts produced by SLM: From causes to consequences, Addit. Manuf. (2018). https://doi.org/10.1016/j.addma.2018.05.005.

[3] J. Drezet, O. Ludwig, M. Rappaz, Un nouveau critère de fissuration à chaud, In Mecamat Infos. 22 (1999) 32–40.

[4] J. Liu, S. Kou, Crack susceptibility of binary aluminum alloys during solidification, Acta Mater. 110 (2016) 84–94. https://doi.org/10.1016/j.actamat.2016.03.030.

[5] J.H. Martin, B.D. Yahata, J.M. Hundley, J.A. Mayer, T.A. Schaedler, T.M. Pollock, 3D printing of high-strength aluminium alloys, Nature. 549 (2017) 365–369. https://doi.org/10.1038/nature23894.

[6] M. Opprecht, J.P. Garandet, G. Roux, C. Flament, M. Soulier, A solution to the hot cracking problem for aluminium alloys manufactured by laser beam melting, Acta Mater. 197 (2020) 40–53. https://doi.org/10.1016/j.actamat.2020.07.015.

[7] K. Schmidtke, F. Palm, A. Hawkins, C. Emmelmann, Process and mechanical properties: Applicability of a scandium modified Al-alloy for laser additive manufacturing, Phys. Procedia. 12 (2011) 369–374. https://doi.org/10.1016/j.phpro.2011.03.047.

[8] S. Kou, A criterion for cracking during solidification, Acta Mater. 88 (2015) 366–374. https://doi.org/10.1016/j.actamat.2015.01.034.

[9] N. Wang, S. Mokadem, M. Rappaz, W. Kurz, Solidification cracking of superalloy single- and bi-crystals, Acta Mater. 52 (2004) 3173–3182. https://doi.org/10.1016/j.actamat.2004.03.047.

[10] T. Clyne, G. Davies, Comparison between experimental data and theoretical pre- dictions relating to dependence of solidification cracking on composition, Solidif. Cast. Met. (1979) 275–278.

[11] M. Rappaz, J. Drezet, M. Gremaud, A New Hot-Tearing Criterion, Metall. Mater. Trans. A. 30 (1999) 449–455.

[12] M.L. Montero Sistiaga, R. Mertens, B. Vrancken, X. Wang, B. Van Hooreweder, J.P. Kruth, J. Van Humbeeck, Changing the alloy composition of Al7075 for better processability by selective laser melting, J. Mater. Process. Technol. 238 (2016) 437–445. https://doi.org/10.1016/j.jmatprotec.2016.08.003.

[13] R. Casati, M. Coduri, M. Riccio, A. Rizzi, M. Vedani, Development of a high strength Al–Zn–Si–Mg–Cu alloy for selective laser melting, J. Alloys Compd. 801 (2019) 243–253. https://doi.org/10.1016/j.jallcom.2019.06.123.

[14] V. Knežević, J. Balun, G. Sauthoff, G. Inden, A. Schneider, Design of martensitic/ferritic heat-resistant steels for application at 650 °C with supporting thermodynamic modelling, Mater. Sci. Eng. A. 477 (2008) 334–343. https://doi.org/10.1016/j.msea.2007.05.047.

[15] F. Tancret, Computational thermodynamics, Gaussian processes and genetic algorithms: Combined tools to design new alloys, Model. Simul. Mater. Sci. Eng. 21 (2013). https://doi.org/10.1088/0965-0393/21/4/045013.

[16] A. Deschamps, F. Tancret, I.E. Benrabah, F. De Geuser, H.P. Van Landeghem, Combinatorial approaches for the design of metallic alloys, Comptes Rendus Phys. 19 (2018) 737–754. https://doi.org/10.1016/j.crhy.2018.08.001.

[17] Q. Zhang, M. Mahfouf, J.R. Yates, C. Pinna, G. Panoutsos, S. Boumaiza, R.J. Greene, L. De Leon, Modeling and optimal design of machining-induced residual stresses in aluminium alloys using a fast hierarchical multiobjective optimization algorithm, Mater. Manuf. Process. 26 (2011) 508–520. https://doi.org/10.1080/10426914.2010.537421.

[18] P. Das, S. Mukherjee, S. Ganguly, B.K. Bhattacharyay, S. Datta, Genetic algorithm based optimization for multi-physical properties of HSLA steel through hybridization of neural network and desirability function, Comput. Mater. Sci. 45 (2009) 104–110. https://doi.org/10.1016/j.commatsci.2008.03.050.

[19] M. Mahfouf, M. Jamei, D.A. Linkens, Optimal design of alloy steels using multiobjective genetic algorithms, Mater. Manuf. Process. 20 (2005) 553–567. https://doi.org/10.1081/AMP-200053580.

[20] P. Konda Gokuldoss, Design of next-generation alloys for additive manufacturing, Mater. Des. Process. Commun. 1 (2019) 19–22. https://doi.org/10.1002/mdp2.50.

[21] N.J. Harrison, I. Todd, K. Mumtaz, Reduction of micro-cracking in nickel superalloys processed by Selective Laser Melting: A fundamental alloy design approach, Acta Mater. 94 (2015) 59–68. https://doi.org/10.1016/j.actamat.2015.04.035.

[22] H.E. Sabzi, S. Maeng, X. Liang, M. Simonelli, N.T. Aboulkhair, P.E.J. Rivera-Díaz-del-Castillo, Controlling crack formation and porosity in laser powder bed fusion: Alloy design and process optimisation, Addit. Manuf. 34 (2020). https://doi.org/10.1016/j.addma.2020.101360.

[23] GRANTA EDUPACK database, (n.d.). https://grantadesign.com/education/ces-edupack/.

[24] N.T. Aboulkhair, M. Simonelli, L. Parry, I. Ashcroft, C. Tuck, R. Hague, 3D printing of Aluminium alloys: Additive Manufacturing of Aluminium alloys using selective laser melting, Prog. Mater. Sci. 106 (2019) 100578. https://doi.org/10.1016/j.pmatsci.2019.100578.

[25] L. Girelli, M. Tocci, M. Gelfi, A. Pola, Study of heat treatment parameters for additively manufactured AlSi10Mg in comparison with corresponding cast alloy, Mater. Sci. Eng. A. 739 (2019) 317–328. https://doi.org/10.1016/j.msea.2018.10.026.

[26] T. Yang, T. Liu, W. Liao, E. MacDonald, H. Wei, C. Zhang, X. Chen, K. Zhang, Laser powder bed fusion of AlSi10Mg: Influence of energy intensities on spatter and porosity evolution, microstructure and mechanical properties, J. Alloys Compd. 849 (2020) 156300. https://doi.org/10.1016/j.jallcom.2020.156300.

[27] A.H. Maamoun, Y.F. Xue, M.A. Elbestawi, S.C. Veldhuis, The effect of selective laser melting process parameters on the microstructure and mechanical properties of Al6061 and AlSi10Mg alloys, Materials (Basel). 12 (2018). https://doi.org/10.3390/ma12010012.

[28] R.S. Mishra, S. Thapliyal, Design approaches for printability-performance synergy in Al alloys for laser-powder bed additive manufacturing, Mater. Des. 204 (2021) 109640. https://doi.org/10.1016/j.matdes.2021.109640.

[29] J.D. Embury, D.. Lloyd, T.R. Ramachandran, Strengthening Mechanisms in Aluminum Alloys, 31 (1989) 579–601. https://doi.org/10.1016/b978-0-12-341831-9.50027-9.

[30] J. Zander, R. Sandström, One parameter model for strength properties of hardenable aluminium alloys, Mater. Des. 29 (2008) 1540–1548. https://doi.org/10.1016/j.matdes.2008.02.001.

[31] G.F. Vander Voort, Atlas of time-temperature diagrams for nonferrous alloys, 1991.

[32] T.. Akopyan, N.. Below, Approaches to the design of the new high-strength casting aluminium alloys of 7xxx series with high iron content, Met. Process. (2016). https://doi.org/http://dx.doi.org/10.17580/nfm.2016.01.04.

[33] Z. Sun, X. Tan, C. Wang, M. Descoins, D. Mangelinck, S.B. Tor, E.A. Jägle, S. Zaefferer, D. Raabe, Reducing hot tearing by grain boundary segregation engineering in additive manufacturing: example of an AlxCoCrFeNi high-entropy alloy, Acta Mater. 204 (2021) 116505. https://doi.org/10.1016/j.actamat.2020.116505.

[34] J. Zander, R. Sandström, L. Vitos, Modelling mechanical properties for non-hardenable aluminium alloys, Comput. Mater. Sci. 41 (2007) 86–95. https://doi.org/10.1016/j.commatsci.2007.03.013.

[35] G.P.M. Leyson, L.G. Hector, W.A. Curtin, Solute strengthening from first principles and application to aluminum alloys, Acta Mater. 60 (2012) 3873–3884. https://doi.org/10.1016/j.actamat.2012.03.037.

[36] S. Ji, D. Watson, Z. Fan, M. White, Development of a super ductile diecast Al-Mg-Si alloy, Mater. Sci. Eng. A. 556 (2012) 824–833. https://doi.org/10.1016/j.msea.2012.07.074.

[37] J. da Costa Teixeira, D.G. Cram, L. Bourgeois, T.J. Bastow, A.J. Hill, C.R. Hutchinson, On the strengthening response of aluminum alloys containing shear-resistant plate-shaped precipitates, Acta Mater. 56 (2008) 6109–6122. https://doi.org/10.1016/j.actamat.2008.08.023.

[38] R.L. Fleischer, Substitutional solution hardening, Acta Metall. 11 (1963) 203–209. https://doi.org/10.1016/0001-6160(63)90213-X.

[39] R. Labusch, A Statistical Theory of Solid Solution Hardening, Phys. Status Solidi. 41 (1970) 659–669. https://doi.org/10.1002/pssb.19700410221.

[40] I. Toda-Caraballo, P.E.J. Rivera-Díaz-Del-Castillo, Modelling solid solution hardening in high entropy alloys, Acta Mater. 85 (2015) 14–23. https://doi.org/10.1016/j.actamat.2014.11.014.

[41] I. Toda-Caraballo, A general formulation for solid solution hardening effect in multicomponent alloys, Scr. Mater. 127 (2017) 113–117. https://doi.org/10.1016/j.scriptamat.2016.09.009.

[42] V.A. Lubarda, On the effective lattice parameter of binary alloys, Mech. Mater. 35 (2003) 53–68. https://doi.org/10.1016/S0167-6636(02)00196-5.

[43] I. Toda-Caraballo, J.S. Wróbel, S.L. Dudarev, D. Nguyen-Manh, P.E.J. Rivera-Díaz-Del-Castillo, Interatomic spacing distribution in multicomponent alloys, Acta Mater. 97 (2015) 156–169. https://doi.org/10.1016/j.actamat.2015.07.010.

[44] H.A. Moreen, R. Taggart, D.H. Polonis, A model for the prediction of lattice parameters of solid solutions, Metall. Trans. 2 (1971) 265–268. https://doi.org/10.1007/BF02662668.

[45] M.F. Ashby, Y.J.M. Bréchet, D. Cebon, L. Salvo, Selection strategies for materials and processes, Mater. Des. 25 (2004) 51–67. https://doi.org/10.1016/S0261-3069(03)00159-6.

[46] J. Masse, L. Cervi, S. Kempa, ALUMINIUM ALLOY FOR LASER WELDING WITHOUT FILLER WIRE, US 2020/0114468 A1, 2020. https://worldwide.espacenet.com/publicationDetails/originalDocument?CC=US&NR=2020114468A1&KC=A1&FT=D&ND=3&date=20200416&DB=EPODOC&locale=fr_EP#.

[47] A. Aversa, M. Lorusso, G. Cattano, D. Manfredi, F. Calignano, E.P. Ambrosio, S. Biamino, P. Fino, M. Lombardi, M. Pavese, A study of the microstructure and the mechanical properties of an Al-Si-Ni alloy produced via selective laser melting, J. Alloys Compd. 695 (2017) 1470–1478. https://doi.org/10.1016/j.jallcom.2016.10.285.

[48] Z. Bian, Y. Liu, S. Dai, Z. Chen, M. Wang, D. Chen, H. Wang, Regulating microstructures and mechanical properties of Al–Fe–Ni alloys, Prog. Nat. Sci. Mater. Int. 30 (2020) 54–62. https://doi.org/10.1016/j.pnsc.2019.12.006.

[49] T. Mukherjee, J.S. Zuback, A. De, T. DebRoy, Printability of alloys for additive manufacturing, Sci. Rep. 6 (2016) 1–8. https://doi.org/10.1038/srep19717.

[50] L. Thijs, K. Kempen, J.P. Kruth, J. Van Humbeeck, Fine-structured aluminium products with controllable texture by selective laser melting of pre-alloyed AlSi10Mg powder, Acta Mater. 61 (2013) 1809–1819. https://doi.org/10.1016/j.actamat.2012.11.052.